ADVANCED MATERIALS INTERFACES
www.advmatinterfaces.de

Fast and Simple Fabrication of Multimaterial Hierarchical Surfaces Using Acoustic Assembly Photopolymerization (AAP)

*Ketki M. Lichade and Yayue Pan**

Multimaterial surfaces with hierarchical features have many potential applications in self-cleaning, droplet manipulation, microfluidics, and biomedicine, owing to their wide range of functionalities induced by structural and material contrasts. Here, a fast and sustainable manufacturing method, acoustic assembly photopolymerization (AAP), is presented for productions of such surfaces. In the novel AAP process, an external acoustic field is used to assemble microparticles to microsized patterns, while the photocuring is combined with the acoustic assembly to produce multilevel hierarchical features, such as cones and wrinkles ranging from nanometer to micrometer. The mechanism underlying the proposed multimaterial surface structuring technique is discussed, and the relationship between process parameters and surface structures is modeled. Effects of surface material composition patterns and surface topology on the hydrodynamic properties are studied. To demonstrate potential applications, three microreactors are designed and automated droplet manipulations are demonstrated. The application of the proposed surface manufacturing approach is further extended to fog harvesting. The AAP technology and the fabricated multimaterial hierarchically-structured surfaces demonstrated in this study can be employed in many other advanced applications in microfluidics, tissue engineering, and also potentially many other fields such as mechanical systems and battery systems.

1. Introduction

Engineered surfaces with preprogrammed properties to perform autonomous tasks are highly desired in a wide range of fields. In particular, multimaterial and hierarchically-structured surfaces exhibit pre-programmed wettability patterns.[1,2] Such patterned surface wettability enables remarkable control over hydrodynamic behaviors without requiring any external power, contributing to many potential uses such as spatial control of fluid, drug delivery, droplet manipulation, water-harvesting, and lab-on-a-chip devices.[3–8] Additionally, these surfaces were also found to be beneficial for biomedical applications such as drug screening and tissue engineering, owing to their shorter reaction times and less usage of rare biological samples or reagents.

A variety of approaches have been developed for the fabrication of multimaterial and/or hierarchically structured surfaces with wettability contrast, including CNC machining,[5] spray coating,[9,10] wire electrical discharge machining,[11] vapor deposition,[12] lithography,[13] and laser microfabrication.[14,15] Although these techniques have enabled the direct fabrication of surfaces with tunable wetting properties, significant challenges still exist in producing complex 3D surface structures in an eco-friendly fashion. For example, hierarchical surfaces developed by the spray coating method undergo chemical instability after exposure to organic solvents. Machining and laser-based manufacturing processes are limited to single materials such as elastomers or metals. Moreover, the surface structure topology fabricated using a conventional direct fabrication approach is usually limited to one or two levels only.

Combining two or more direct fabrication techniques is a common approach to address the aforementioned challenges and achieve higher structural complexities. For instance, Lee et al.[16] prepared microscale groove surface patterns using machining and compression molding, resulting in a superhydrophobic anisotropic surface (CA:150°). Additional dip-coating created nanoscale patterns to induce low sliding angles, enabling liquid transportation. Peng et al.[17] utilized templating and diffusion-controlled bucking to generate a dual-structured hierarchical surface with microsized wrinkles. To enhance the biocompatibility, the surface was chemically modified using dopamine-glycopolymer. Other indirect micro-fabrication methods, including surface wrinkling by thermal annealing,[18] electrochemical etching followed by deposition,[19] and colloidal crystal templating,[20] have been investigated for developing hierarchical surfaces with a high wettability contrast. Nevertheless, it is difficult to precisely control the dimensions of the

K. M. Lichade, Y. Pan
Department of Mechanical and Industrial Engineering
University of Illinois at Chicago
Chicago, IL 60607, USA
E-mail: yayuepan@uic.edu

The ORCID identification number(s) for the author(s) of this article can be found under https://doi.org/10.1002/admi.202201981.

DOI: 10.1002/admi.202201981

surface features in all those fabrication methods. These indirect manufacturing processes involve complicated processing steps, expensive equipment, hazard chemicals, and a long fabrication time. Moreover, chemical modification has limited durability, and chemical etching involves generation of chemical waste which causes environmental sustainability problems.

In contrast, additive manufacturing (AM) techniques such as stereolithography (SL)[21] and Two-Photon Polymerization (TPP)[22] have emerged as advanced and direct manufacturing techniques for the fabrication of complex 3D hierarchical surfaces via layer-by-layer approach. In addition, to fabricate surfaces with spatially-varied material compositions, several studies have demonstrated that the use of external forces through magnetic,[23,24] acoustic,[25,26] or electrical[27] signals can precisely control the location and concentration of particles within the polymer matrix. For instance, the magnetic field-assisted SL process demonstrated by Lu et al.[23] can fabricate heterogeneous composite structures with locally-controlled magnetic particle distribution. A major limitation of magnetic and electric field-assisted processes is that the particles have to be naturally responsive to the external field, limiting the particle selection range. In contrast, the acoustic field-assisted particle patterning only requires the density difference between particles and liquid polymer. There is little constraint on particle shape, size, or property. Previously, our group had demonstrated the use of the acoustic field to pattern tungsten, aluminum, titanium, and copper particles which are nano- or micro-size.[28] Additionally, other works in literature have utilized acoustic field to pattern nanoparticles, nano-rods, and fibers.[29] For instance, Asif et al.[29] and Greenhall et al.[30] utilized acoustic field and SL to fabricate patterned composite surfaces with enhanced mechanical strength and electrical conductivity. However, the primary focus of these field-assisted AM processes was to fabricate composite structures with the spatially-designed material distribution for enhanced mechanical or electrical properties. Despite the recent advances in AM technology, it remains challenging to produce surfaces characterized by both the spatially-designed material distribution and multiscale hierarchical features. To the author's best knowledge, no study has investigated the ability of an external field and light-assisted photopolymerization technique to fabricate hierarchically-structured surfaces with spatially-varied material composition.

This paper reports a simple, fast, cost-effective, and environmentally sustainable approach for fabricating multimaterial surfaces covered by macro, micro, and nanoscale features. This manufacturing approach is based on the strategic integration of acoustic-field-assisted particle patterning and ultraviolet (UV) photopolymerization, which we call as acoustic assembly photopolymerization (AAP). Details of the manufacturing process and experimental setup are given in Section 2. The novel AAP approach is investigated for fabricating a 3-level hierarchical surface design consisting of multimaterial patterns, cones, and wrinkle structures. To validate the effectiveness of the AAP process on engineering surfaces for hydrodynamic-related applications, systematic studies of the fabricated surfaces' wettability have been conducted. Results are analyzed in Section 3. Additionally, several practical applications are demonstrated in Section 3, such as microreactors for small volume liquid manipulation, and fog harvesting capability. The novel APP technique developed in this study shows great potential and is advantageous for surface engineering for various applications that require tunable wettability, including microfluidic systems and biomedical devices.

2. Experimental Section

2.1. Experimental Setup

The schematic of the AAP testbed developed in this work is shown in **Figure 1**. The main components of the system included an off-the-shelf projector, resin vat, piezoelectric plates, signal generator, and amplifier. Two pairs of rectangular-shaped piezoelectric plates (Steiner and Martins, Inc.) were

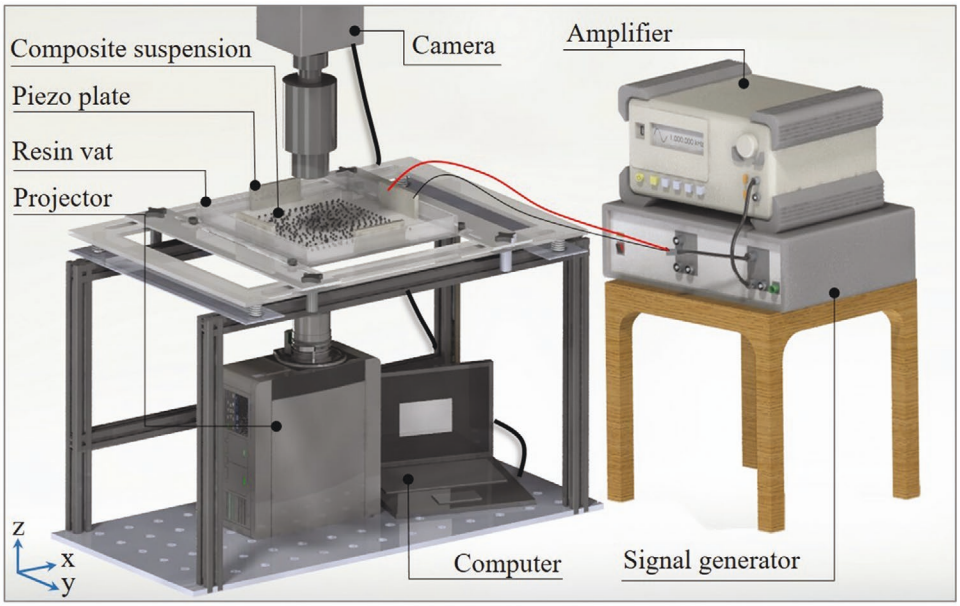

Figure 1. Schematic of acoustic assembly photopolymerization (AAP) setup.

Table 1. Properties of polymer and particle.

Polymer properties		Particle properties	
SPOT-E elastic		Iron oxide powder	
Color	Transparent yellow	Color	Black
Density	1.12 g cm^{-3}	Density	0.51 g cm^{-3}
Dynamic viscosity	0.1 Pa s	Size	0.3 µm

attached to the vertical walls of the acrylic resin vat. The bottom of the resin vat was covered with transparent polyethylene terephthalate (PET) film (thickness: 175 µm). A high-speed camera was integrated to monitor the patterning accuracy. The acoustic field was actuated using an AC signal generated from a function generator (RIGOL Technologies Inc., Beijing, China) and amplified using an amplifier (TEGAM Inc., Geneva, OH). A UV projector was placed underneath the resin vat to solidify the liquid resin with microparticle patterns.

Spot-E elastic (Spot-A Materials, Sonnaya Ulitka S. L., Barcelona, Spain) was used as a base material in this study. Furthermore, owing to easy availability, low cost, non-toxic nature, and high mechanical strength, iron oxide magnetic particles (MPs) (Alpha Chemical, USA) were used as functional fillers in the following test cases.[31,32] Material properties were summarized in **Table 1**. Homogeneous particle-resin suspensions with the desired concentration of the MPs were prepared according to the method given in the previous study.[33] It was known that the higher loading fraction of microparticles in the particle-resin suspension leads to a higher suspension viscosity.[11] However, higher viscosity fluid increased the undesired drag forces during acoustic patterning.[34] Therefore, to meet the viscosity requirement for successful pattern formation, the weight ratio of the microparticles used in this study was limited to 5 wt%.

2.2. Multimaterial Hierarchical Surface Fabrication Using AAP

Existing literature on acoustic patterning showed that various micro/nanoparticle patterns could be achieved using different shapes of piezoelectric elements, including ring, rectangle, and disc.[28,35,36] To validate the manufacturing process, the simple rectangular piezoelectric plate was used to generate line and dot patterns, which were commonly used in engineering applications.[37,38] With the integration of piezoelectric plates in resin vat, three types of particle distributions can be generated in the liquid resin during the manufacturing process: 1) homogeneously distributed patterns without acoustic actuation, 2) line particle patterns by actuating a pair of opposite plates, and 3) dot patterns by actuating a pair of adjacent plates.

To fabricate a hierarchically-structured particle-polymer composite surface, a five-step manufacturing procedure is shown in **Figure 2**a: Step 1: Filling the vat with the prepared particle-polymer suspension. Step 2: Actuating the piezoelectric plates properly to pattern and assemble microparticles in the liquid polymer. Step 3: Projecting digital mask images onto the bottom surface of the vat for a few seconds to cure the area with the desired geometry. Step 4: Turning off the UV light projection and the acoustic field and peeling the cured layer off from the vat bottom surface. Step 5: Cleaning the cured sample using ethanol. Figure 2b shows the schematics of a multilevel hierarchically-structured particle-polymer composite surface proposed in this study: Level-1 showed the surface topology of the entire film, which was composed of multimaterial microparticle grooves and a pure polymer plateau. Subsequently, Level-2 showed the surface topology of the groove and plateau region at a smaller scale. It can be seen that each micro-plateau was composed of clusters of microcones, which were formed by the non-uniform curing due to the light-blocking effect of microparticles. Level-3 showed that each microcone was covered by nanowrinkles. The nanowrinkle formation was possibly attributed to the aggregation of microcones after solidifying for an adequate time (within seconds).

2.3. Investigation of Acoustic Patterning

To create desired particle patterns in liquid resin, the acoustic particle patterning process must be understood and characterized. In this work, two sets of piezoelectric plates were

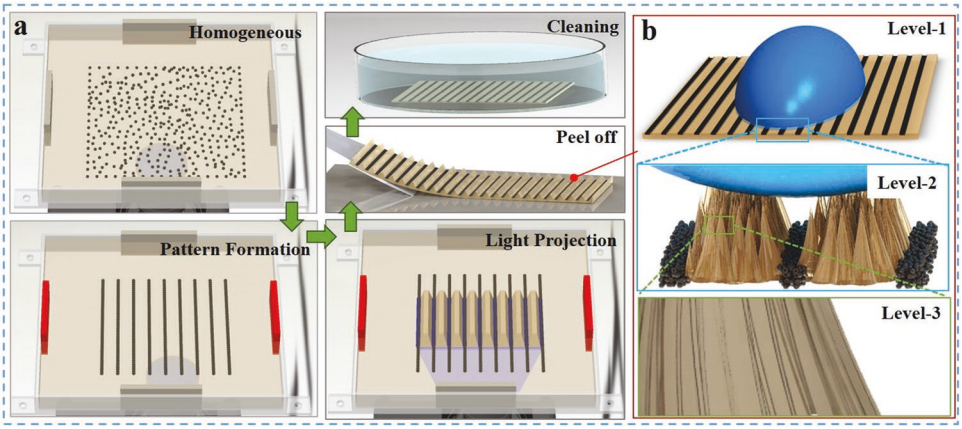

Figure 2. a) Procedure for the fabrication of multimaterial surfaces with hierarchical features. b) Multilevel surface structuring: i) Level-1: the entire film showing groove and plateau; ii) Level-2: the plateau regions are composed of clusters of microcones; iii) Level-3: each microcone is covered by nanowrinkles.

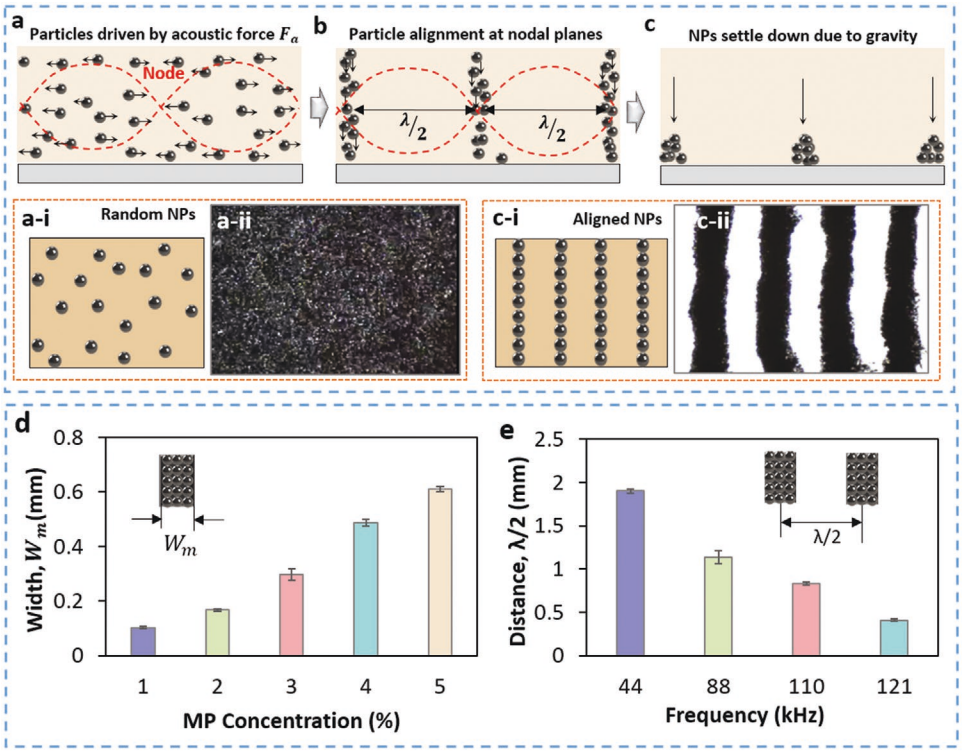

Figure 3. a) Homogeneously distributed particles move toward acoustic nodes within the resin vat. b) With the actuation of the acoustic field, a strong acoustic force applied on MPs enables particle assembling into vertical and parallel stacking. c) Particles accumulate at the bottom of the vat along the nodal planes due to gravity. d) Width of the particle assembly pattern (W_m) generated by using a composite material with different NPs concentrations. e) Distance between adjacent patterns ($\lambda/2$) at different actuation frequencies.

connected opposite to each other to generate two sets of acoustic waves within a homogeneous composite medium. The acoustic radiation forces (F_a) generated by the actuation of piezo plates drive the particles toward the center of the closest acoustic node position, as shown in **Figure 3**a. The acoustic force on a single particle can be modeled as:[34]

$$F_a = -\frac{\pi V_p p_a^2 \beta_f}{2\lambda}\phi \sin\left(\frac{4\pi x}{\lambda}\right) \quad (1)$$

where V_p is the volume of the particle, p_a is the acoustic pressure, λ is the wavelength, β_f is the compressibility of the liquid resin, and ϕ is the contrast factor between particle and resin as shown in Equation (2):

$$\phi = \frac{5\rho_p - 2\rho_f}{2\rho_p + \rho_f} - \frac{\beta_p}{\beta_f} \quad (2)$$

where ρ_p is the particle density, ρ_f is the resin density, and β_p is the compressibility of particles. Since each nodal plane was equally spaced by half of the acoustic signal wavelength (λ), the distance between adjacent particle patterns was $\lambda/2$ (Figure 3b). In this work, for the selected particle-polymer composites, the values of V_p, ρ_p, ρ_f were 0.085 μm^3, 1.12 g cm^{-3}, 0.51 g cm^{-3}, respectively. After the acoustic patterning, the particles assembled and settled down at the bottom of the resin vat due to gravity, resulting in a Level-1 structure, as shown in Figure 3c.

To characterize the acoustic signal wavelength (λ) value, the relationship among material properties, acoustic process parameters, and particle patterning was experimentally validated. The overall patterning time used in this work was ≈10 s (see Movie S1, Supporting Information). As shown in Figure 3d, the width (W_m) of the assembled particle pattern can be modulated by adjusting the magnetic particle concentration within the photocurable composite material. Furthermore, the distance between two adjacent patterns was equal to half of the acoustic signal wavelength (λ), which can be adjusted by varying the actuation frequency. The experimental characterizations are plotted in Figure 3e. With the process parameter settings and materials used in this study, the pattern width (W_m) can be varied from 0.1 to 0.62 mm, and the distance between adjacent patterns ($\lambda/2$) can be adjusted in the range of 0.4 to 1.5 mm.

2.4. Investigation of Gradient Particle Distribution

The gradient acoustic force applied to particles enabled a particle concentration gradient along the particle assembly, as illustrated in **Figure 4**a. In the areas closer to the node, the acoustic force was the maximum, enabling the highest particle packing density at the center of the particle pattern and the particle density gradually decreased from the center toward the edge. To quantitatively characterize the particle assembly density, the material composition of the cured composite samples

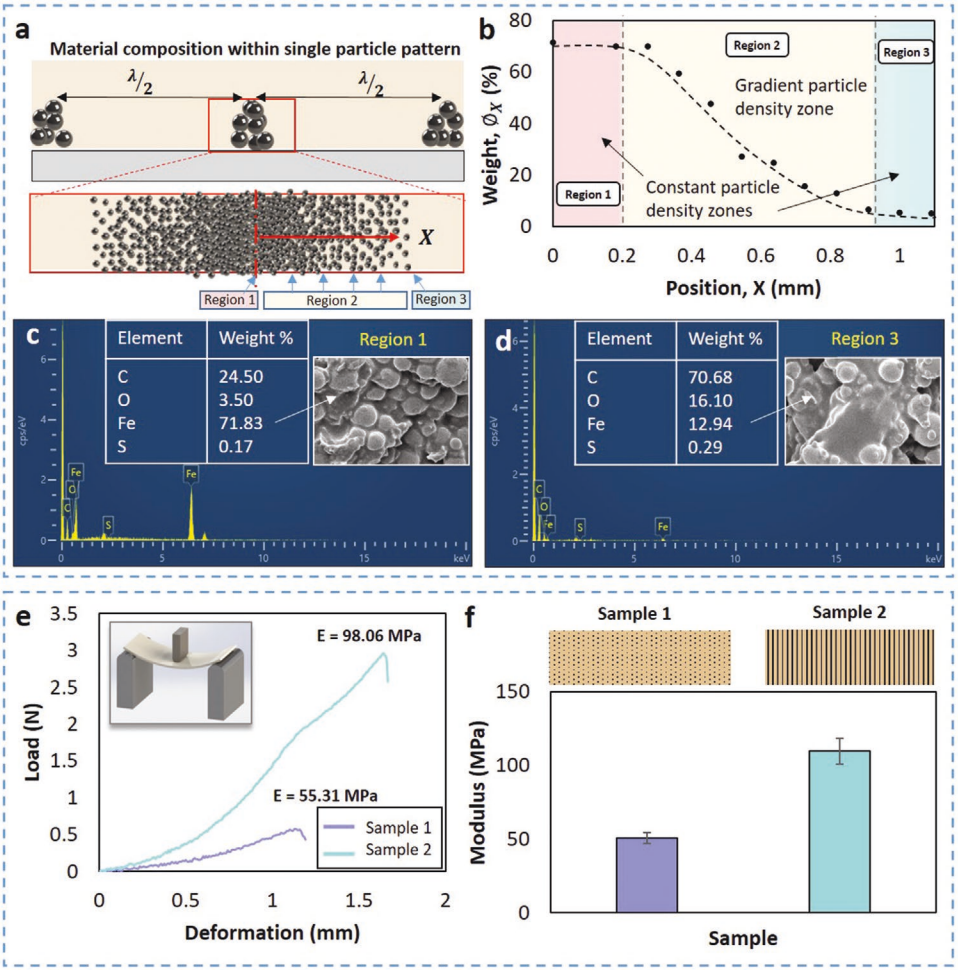

Figure 4. a) Schematic of gradient microparticle distribution within a single pattern. b) Results of EDS analysis showing a constant-gradient-constant particle density in the scanned area along a single pattern. c) EDS point-scan spectrum at the center of the pattern (region 1 in (b)). d) EDS point-scan spectrum at the edge of the pattern (region 3 in (b)). e) Three-point bending tests force-displacement curves for homogeneous and line patterned surfaces, f) schematic of sample 1 (homogeneous), sample 2 (line pattern), and comparison of young's modulus.

was characterized using energy-dispersive spectroscopy (EDS) (JEOL JSM-IT500HR FESEM). A dimensionless position was defined as $X = x/W_m$, where x is the position of the microparticle from the pattern center. The data was extracted from the EDS point scan. Accordingly, the concentration of particles ($\varnothing_X$) in the composite was calibrated and plotted corresponding to its dimensionless position within a single particle assembly pattern, as shown in Figure 4b.

Initially, the feedstock was a homogeneous composite resin containing uniformly distributed particles (particles: 5 wt%, resin: 95 wt%). Particles moved toward the nodal areas, resulting in region 1, which contained the highest microparticle concentration. Furthermore, due to the acoustic force gradient, the particle concentration smoothly decreased from the node toward the antinode. This region was marked as region 2 in Figure 4b. Finally, a nearly uniform distribution with the lowest microparticle concentration can be observed in region 3. Ideally, this region should not contain any microparticle. However, since the resin viscosity was high, a small portion of magnetic particles might stay in the region. This effect can be eliminated by using resin with a lower viscosity to reduce the viscous drag.

The gradient in microparticle packing density within a single pattern was confirmed by the EDS spot profiles and SEM images. As shown in Figure 4c, the particles were assembled with the highest particle density (71.83 wt%) at the center of the pattern. A gradual reduction in particle concentration was observed at the edge of the pattern (i.e., decreasing from 71.83 to 12.94 wt%), as shown in Figure 4d. In addition, it can be observed from EDS results that region 1 and region 3 had relatively constant particle density, yet these two regions were relatively small, that is, ≈0.2 µm. It is believed that although the particle pattern width was dependent on the acoustic settings and feedstock particle concentration, all acoustic assemblies would exhibit the same three-regions particle distribution pattern, regardless of the process settings and material properties.

It was known that the particle-polymer patterns suffered from low interfacial bonding owing to the different physical properties of the hard particle and soft polymer. The gradient

particle distribution in region 2 could help increase the bonding between polymer and particles. In order to understand the effect of particle distribution on the mechanical properties of the composite surfaces, the bending properties of the line patterned (sample 2) surfaces were tested and compared with the homogeneous (sample 1) surface via a three-point bending measurement. The flexural measurements were performed using a universal testing machine (3360-series, Instron, Norwood, MA) at room temperature with a testing rate of 0.05 mm min^{-1}. The typical sample dimensions were 25 mm × 10 mm × 2 mm. The obtained load-deformation curves and young's modulus are shown in **Figure 5**. Since the maximum deformation at break reduced with an increase in particle concentration, fixed loading of 5 wt% was used to prepare both samples. As shown in Figure 5a, the maximum deformation achieved by sample 1 was 1.19 mm, whereas sample 2 could achieve higher deformation of 1.67 mm. This increase in deformation was a result of a soft polymer matrix surrounding particle patterns. Additionally, the Young's modulus of sample 2 was 2.2 times higher than homogeneous sample 1, as shown in Figure 5b. The increased mechanical properties of the line patterned surfaces, particularly modulus, indicated that the particles were strongly bonded to the polymer matrix.

2.5. Investigation of Curing Characteristics

The Level-2 cluster of conical feature formation was not solely governed by the acoustic assembly of NPs but also by the non-uniform curing of the photopolymer surrounding the NPs assemblies.[39] As discussed in the previous section, the microparticles assembled at acoustic nodes. When the patterned composite was exposed to a UV light projection image, the highly-dense particle patterns blocked the light. While the plateau regions between particle patterns had a very low concentration of particles, it enabled freeform solidification of polymer structures, as shown in Figure 5a. The width of solidified plateau region can be predicted by

$$W_c = \frac{\lambda}{2} - W_m \tag{3}$$

The height of the Level-2 cluster of conical features was a function of the exposure time and material properties, described by the Beer–Lambert law as follows:[40]

$$H_c = D_p * \ln\left(\frac{t}{t_c}\right) \tag{4}$$

where t_c is the critical curing time of liquid resin for initiating the photopolymerization, D_p is the penetration depth, and t is the total exposure time. As discussed in Section 2.3, the gradient distribution of microparticles in region 2 enabled formations of microcones surrounding the pattern. Given a certain exposure time, the solidified microcones aggregated due to surface tension, forming Level-3 nanoscale wrinkles, as shown in Figure 5b. The height of the surrounding microcone solidified with ϕ_X wt% of NPs at position X can be modeled as:[24]

$$H_n = \frac{D_p}{1 + \dfrac{3\phi_X \rho' D_p}{4d\left[100 - \left[1 - \dfrac{\rho'}{\rho}\right]\phi_X\right]\rho}} \ln\left(\frac{t}{t_c}\right) \tag{5}$$

where d is the average diameter of particles, $\varnothing_X$ is the particle concentration at position X (position X is a quantity that measures the distance of particle position from the center of the pattern), and ρ' and ρ are the density of the resin with and without particles, respectively.

To understand the effect of microparticle concentration on the curing characteristics, the cure depth of resin with 0 to 5 wt% MPs was characterized using a single-layer-curing method. Figure 5c shows the schematic of the curing depth experiment. The composite resin was poured into the vat, and a square-shaped mask image (10 × 10 mm) was projected using a UV source for a certain exposure time (20, 30, and 40 s). Owing to the small thickness of the PET film (125 µm), the actual light energy absorbed by composite material was the same as the energy released by the projector (≈20.94 mW), indicating little energy loss. After removing excess liquid resin, the thickness of the solidified layer was measured by a micrometer caliper. The critical curing time t_c for each loading fraction was

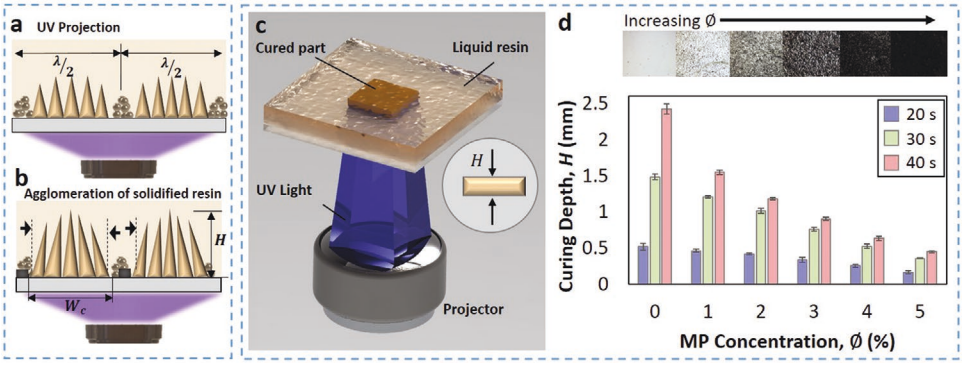

Figure 5. a) During UV projection, the area between microparticle assemblies grows and solidifies, forming the plateau region. b) With adequate exposure time, the surface tension causes the agglomeration of solidified cones in the plateau regions. c) Schematic of curing depth measurement for evaluating polymerization rates of individual resins. d) Curing depth (H) of the pure polymer and composite material with varied MP concentration ($\varnothing$) as a function of UV-light exposure time.

experimentally measured and found to be ranging from 3 s to 16 s. Figure 5d shows the optical images of composite materials with increasing microparticle concentrations and a plot summarizing curing depth results as a function of projection time. By comparing the experimental results with Equation (5), the measured value of D_p for 0, 1, 2, 3, 4, and 5 wt% MPs were 2.73, 1.58, 1.13, 0.83, 0.55 and 0.41 mm. Experiments showed that the curing depth of pure resin was the largest, and the curing depth decreased with the increase of particle concentrations, with the composite material with 5 wt% MPs showing the smallest curing depths.

3. Results and Discussion

3.1. Fabrication of Hierarchical Surfaces and Morphology Characterization

Three samples with varied material compositions and topology were designed and fabricated using the AAP process described in Section 2.2. In this study, the exposure time and microparticle concentration were kept as 40 s and 5 wt%, respectively. The total fabrication time was 50 s, including acoustic patterning for 10 s and light projection for 40 s. The post-processing required additional 2 min, which included cleaning and peeling of the surface. The schematic of the experimental setup and the corresponding SEM images of fabricated surfaces are shown in **Figure 6**. For SEM imaging, the probe current and spot size were set at 5 kV and 4, respectively. To avoid charging during SEM imaging, the samples were sputter-coated with a 10 nm platinum layer.

The homogeneous isotropic surface (HoI) was fabricated by curing the feedstock composite without applying the acoustic field, as illustrated in Figure 6a. The SEM images (Figures 6ai–iii) of the fabricated sample show arrays of microcones, which are formed due to the light-blocking effect of the magnetic particles homogeneously distributed in liquid resin. In contrast, heterogeneous surfaces were fabricated by first actuating piezo plates at a 1.1 MHz frequency to pattern particles and then photocuring, following the procedure described in Section 2.2. To prepare heterogeneous surfaces with an isotropic distribution of microstructures (heterogeneous isotropic samples; HeI), a pair of adjacent piezo plates were actuated, enabling discrete assembly of microparticle at the intersection of orthogonal nodal planes, as illustrated in Figure 6b. After polymerization, the liquid resin between microparticle assemblies was solidified into clusters of microcones, as shown in Figures 6bi–iii. Similarly, heterogeneous anisotropic (HeA) surfaces were fabricated by actuating a pair of opposite piezo plates to assemble microparticle into parallel lines, as illustrated in Figure 6c. After light exposure, the areas between particle lines were solidified into clusters of microcone, forming the plateau regions. The microparticle lines were cured with a much lower depth, forming the groove regions, as shown in Figures 6ci–iii. Additional features such as vertical wrinkles and microcones can be observed on both HeI and HeA samples.

3.2. Joint Effect of Surface Structure and Material Composition on Wetting Properties

3.2.1. Contact Angle of HoI

Material contrast plays a vital role in surface wetting properties. To identify the optimal particle fillers for fabricating composite surfaces for hydrodynamic applications, it is necessary to first understand the nature (hydrophilic or hydrophobic) of composite surfaces with different fillers. In our previous work,

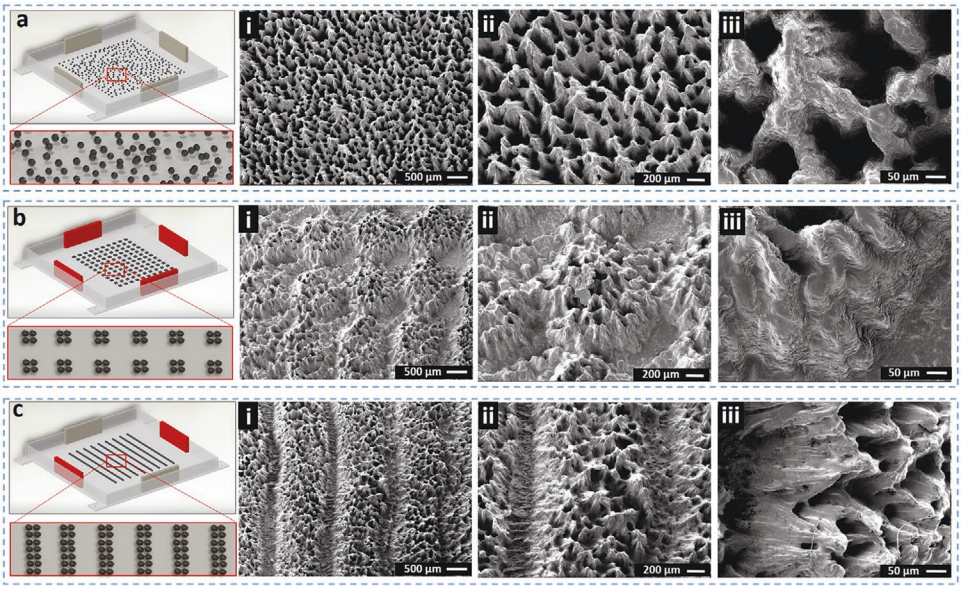

Figure 6. Schematic of the experimental setup and SEM images of the fabricated samples: a) Homogeneous isotropic surface (HoI) without acoustic actuation. b) Heterogeneous isotropic surface (HeI) using a pair of adjacent piezo plates. c) Heterogeneous anisotropic surface (HeA) using a pair of opposite piezo plates.

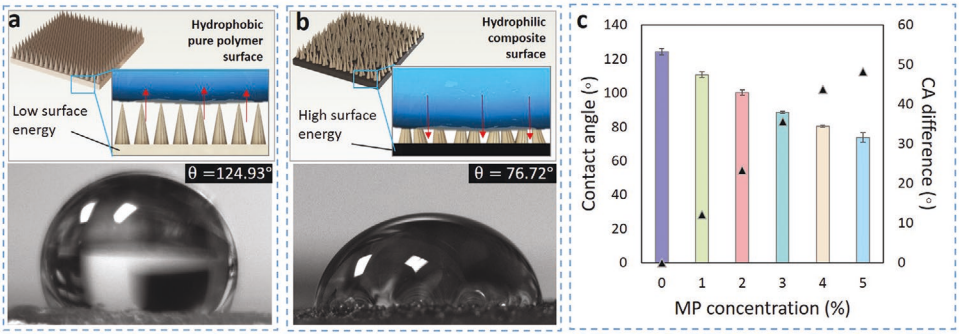

Figure 7. a) Water droplet sitting on the HoI surface fabricated with pure polymer. b) Water droplet sitting on the HoI surface fabricated with composite polymer (5 wt% MPs). c) Contact angle (bars) and wettability difference (points) between composite and pure polymer surfaces.

we found that particle-polymer composites prepared from iron oxide magnetic particles (MPs) exhibit the smallest contact angles than polymer composites embedded of other particles, including copper, diamond, and silver.[33] This gives us the biggest window to tune hydrodynamic properties of the produced particle-polymer composites. Therefore, in this work, we used MPs to show the potential of our novel manufacturing technique in hydrodynamic applications. To further understand the effect of MPs weight ratio on the wettability of the corresponding composite surface, six isotropic surfaces were prepared using 0 to 5 wt% MPs. The wettability of the samples was characterized by measuring the contact angles of distilled water on them. The optical images were taken using a high-definition camera (CMLN-13S2M-CS, Point Grey Research Inc), and the contact angle was measured using ImageJ software.

As shown in **Figure 7**a, the initial contact angle of the surface fabricated using pure resin (0 wt% MPs) was 124.93°, indicating that the resin is hydrophobic in nature. The hydrophobic nature of the surface changed to hydrophilic (<90°) when the concentration of MPs was increased to 5 wt% (76.72°), as shown in Figure 7b. The contact angle difference between pure polymer and 5 wt% composite surfaces was ≈50°, indicating a high surface energy difference (Figure 7c). This trend is in agreement with previously published studies on the wettability of composite surfaces with varied concentrations of MPs.[31,41] Although it is possible to achieve super hydrophilicity by further increasing the microparticle concentration, it was not investigated in this study because suspensions with a higher particle concentration cannot be cured by UV light projection.

3.2.2. Contact Angle of HeI

As discussed in Section 2.2, the geometry of the surface structures can be controlled by changing the acoustic settings or UV light projection time. To study the influence of surface topology on the wetting property, different HeI surfaces were fabricated by varying the UV light projection time, and their water contact angle was measured. The HeI surface fabricated with 20 s exposure time demonstrated lower micro-cone height and hence a relatively smooth surface. By gradually increasing the UV light exposure time from 20 to 40 s, the height of micro-cones on the HeI surface increases, hence the surface roughness. The surface sample fabricated with 20 s exposure time showed a low hydrophobicity with a static contact angle of only 99.22°, as shown in **Figure 8**a. The water droplet creates a much higher contact angle (112°–161°) with the surface fabricated using a higher exposure time (Figure 8c). In particular, the HeI surface with 40 s exposure time showed excellent superhydrophobicity featuring a contact angle of ≈160.54°, as shown in Figure 8b.

According to the Wenzel wetting theory, the contact angle of the prepared surface will increase with an increase in surface roughness if the smooth surface with similar material composition shows a contact angle greater than 90°.[11] For our proposed HeI surface fabricated with a higher exposure time, the

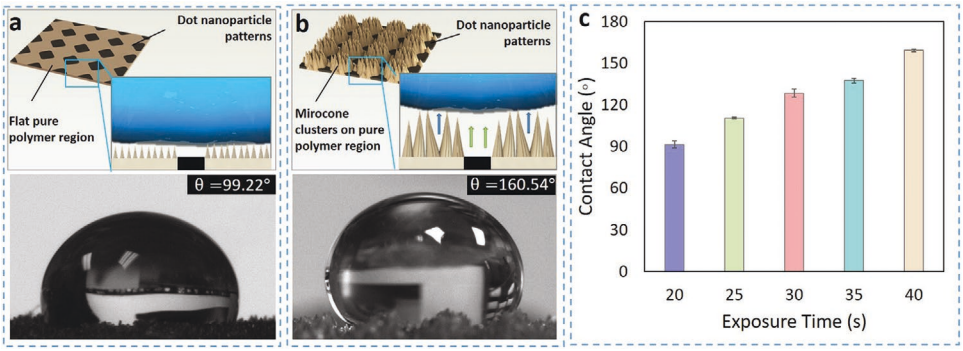

Figure 8. a) Water droplet sitting on the HeI surface fabricated with 20 s exposure time. b) Water droplet sitting on the HeI surface fabricated with 40 s exposure time. c) The contact angle of HeI surfaces as a function of exposure time.

conical clusters of micro-cones and wrinkles along their surface increase the surface roughness. Furthermore, the individual conical clusters create a network of microcavities among the adjacent clusters (green arrow in Figure 8b), and microcones within each cluster create a network of nanocavities (blue arrows in Figure 8b). The dual-scale cavities retain micro to nanosized air bubbles within the structure, which lead to the reduced contact area between surface and water droplet. The formed dual-scale air pockets resulting from the trapped air within and among the clusters prevented the water droplets from seeping through the surface. Therefore, the enhancement in hydrophobicity of the fabricated HeI surfaces can be ascribed to the hierarchical micro/nanoscale surface structures. With the higher exposure time, the heights of microcone structures and conical clusters increase, leading to deeper air pockets and hence larger hydrophobicity.

3.2.3. Contact Angle of HeA

To understand the effect of AAP process parameters on the wetting properties of HeA surfaces, three samples were prepared by varying the UV light exposure time from 20, 30, and 40 s. Prior to projection, the acoustic field was actuated with a voltage of 20 V and a frequency of 1.1 MHz. With the 20 s exposure time, the plateau regions were moderately smooth, with parallel microparticle assembly lines embedded in the groove regions of the surface, as illustrated in **Figure 9**a. On the other hand, at a higher exposure time of the 40 s, the plateau regions are composed of clusters of microcones in parallel conical ridge patterns, as illustrated in Figure 9b. Figure 9a,b shows the optical images of the water droplets from parallel ($\theta_{\parallel}$) (i.e., view plane is parallel to the particle assembly line/grooves), perpendicular ($\theta_{\perp}$) (i.e., view plane is orthogonal to the particle assembly line/grooves), and top view. It can be seen that on the surface, without deep grooves (t = 20 s), the droplet shape was close to spherical. The droplet aspect ratio increased by increasing the exposure time to 40 s, indicated by the highly elongated elliptical shape in Figure 9b. It is because the increased exposure time increases the height of the plateau regions, that is, the height of the micro-cones, while the height of the groove regions changed little. The experimental data indicate that the AAP process parameters can control the surface structure characteristics and hence the droplet shape, enabling tunable anisotropic wetting.

The measured contact angles and anisotropy are summarized in Figure 9c. Upon increasing the exposure time and hence the fabricated conical cluster height, the parallel contact angle $\theta_{\parallel}$ increased, but the perpendicular contact angle $\theta_{\perp}$ decreased. Among the three surfaces plotted in Figure 9c, the surface fabricated with 20 s exposure time has the smallest topology contrast because the height difference between its plateau and groove is the smallest. With the small topology contrast, the surface produced a parallel and a perpendicular contact angle of ≈105°. In contrast, the surface prepared using 40 s exposure time showed the highest surface topology contrast as its plateau regions are much higher than its groove regions. Accordingly, the larger surface topology contrast leads to a higher parallel contact angle and a lower perpendicular contact angle of 139° and 52°, respectively, compared to the other two surfaces. This is because the droplet was trapped on the edges of conical clusters, which led to the squeezing and pinning of the droplet in the direction perpendicular to the groove. Additionally, the hydrophilic composite material in the groove regions between plateaus (i.e., which consists of conical clusters) provided enough Laplace pressure and surface energy gradient for the droplet to stretch along the groove direction. The resulting wetting anisotropy along parallel and perpendicular directions was as high as 87°, indicating their potential for directional water transport and droplet spreading applications.

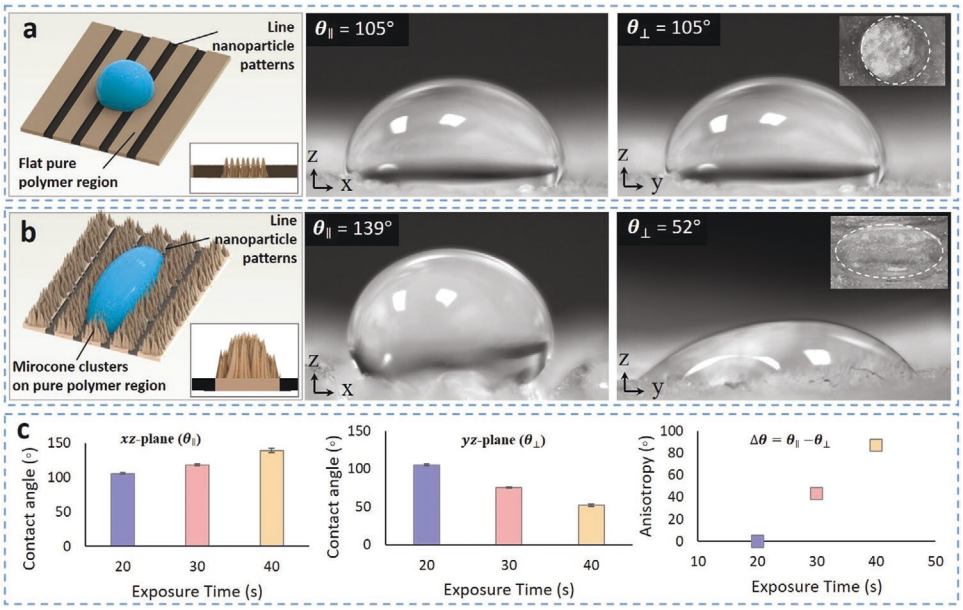

Figure 9. a) Water droplets sitting on the HeA surface fabricated with 20 s exposure time. b) Water droplets sitting on the HeA surface fabricated with 40 s exposure time. c) Contact angles along the parallel and perpendicular direction and measured anisotropy with respect to the exposure time.

3.3. Test Case 1: Self-Driven Microreactors

Tunable and efficient mixing of chemical or reagent droplets is essential for micro-analysis systems used in the biomedical field, particularly microreactors for bio-assays.[42] Many studies have investigated different approaches for droplet manipulation using external forces, including temperature gradient,[42] magnetic field,[43] and NIR light.[44] However, these indirect techniques require manual interference and are limited to one-directional manipulation. Furthermore, the reaction enabled by external forces may not be the same as the actual reaction due to external disturbances such as heat released or environmental condition variations. To demonstrate the practical applications of the proposed manufacturing technique, several microreactor devices are prepared in this study using HoI, HeI, and HeA surfaces and the AAP manufacturing technique. As models for demonstration, KOH (Sigma-Aldrich, St. Louis, MO) and phenolphthalein (Sigma-Aldrich, St. Louis, MO) aqueous droplets were chosen to study droplet manipulation in the prepared microreactor chip. The volume of droplets was between 6–10 µL.

To demonstrate the controllable wetting and bi-directional reaction, a rectangular-shaped HeA surface was fabricated with gradient wettability along its length (x–direction). To fabricate such a HeA surface with gradient wettability, the exposure time was gradually increased from 20 to 40 s along the length of the surface (x–direction), where the center was exposed for the maximum time, 40 s. Therefore, for a surface with a length of L along the x–direction, the plateau regions at the edges (close to $x = 0$ and close to $x = L$) were moderately smooth ($\Delta\theta = 0°$) with a gradual increase in topology contrast, that is, cone height, toward the center of the surface ($x = L/2$) ($\Delta\theta = 87°$). In this way, the directional motion of droplets from edges to center (from $x = 0$ to $x = L/2$, and from $x = L$ to $x = L/2$) could be achieved. This microreactor design is based on the joint effect of the material contrast (between composite in the groove regions and polymer in the plateau regions) and the gradient surface topology contrast (i.e., gradient height difference between the grooves and the micro-cone clusters in plateau regions) of the HeA surface, as illustrated in **Figure 10**a. The gray color represents particle-polymer composite, which is hydrophilic naturally. The tan color represents pure polymer, which is hydrophobic naturally. The tan-colored regions are plateaus, which are composed of clusters of micro-cones and higher than the groove regions. In the middle of the surface ($x = L/2$), the micro-cones in the plateau region are the highest, and accordingly, the plateau is the roughest. The height of micro-cones and the roughness of plateau regions decrease gradiently from the center toward the edges ($x = 0$ and $x = L$). Such gradient surface topology contrast combined with the composite-polymer material wettability contrast, enabling gradient wettability and hence automatic droplet motions and reactions without applying any external forces.

The automatic droplet reaction function of the fabricated surface is tested. Two droplets were simultaneously placed on the surface at ≈ 6 mm apart. Owing to the gradient wettability, two droplets spread face-to-face toward the center and merged into one within 52 s. The entire droplet finally became pink, indicating a 100% chemical reaction (see Movie S2, Supporting Information). Notably, pinning was observed on the opposite side due to the negligible anisotropic wetting at the edges of the microreactor.

While faster reactions are required for chemical diagnosis, slower reactions with controlled diffusion of chemicals can be useful in identifying the optimum concentration of solvents in specific reactions. Therefore, to demonstrate a unidirectional diffusion-based microreactor, we have designed another device composed of gradient HeA surface and HeI surface and demonstrated its use as a unidirectional diffusion-based microreactor, as shown in Figure 10b. Note that it is a single film fabricated by AAP. The left side of the film consists of gradient HeA surface structure, serving as a chemical release surface via grooves. The right side is made of the HeI surface structure, serving as a reaction chip. The reaction started at 3 s, where the phenolphthalein on the left HeA surface slowly diffused into the KOH droplet on the right, indicated by the change in color and droplet sizes (see Movie S3, Supporting Information). The transfer rate can be calculated by monitoring the change in the volume of the aqueous phenolphthalein droplet. The overall time for 100% reaction on a unidirectional reactor was 1.7 times longer than a bi-directional microreactor.

3.4. Test Case 2: Droplet Transportation

Next, we fabricated a device to collect and transfer droplets along the z–direction using two different surfaces. Due to its high surface energy, the hydrophilic HoI surface was used as

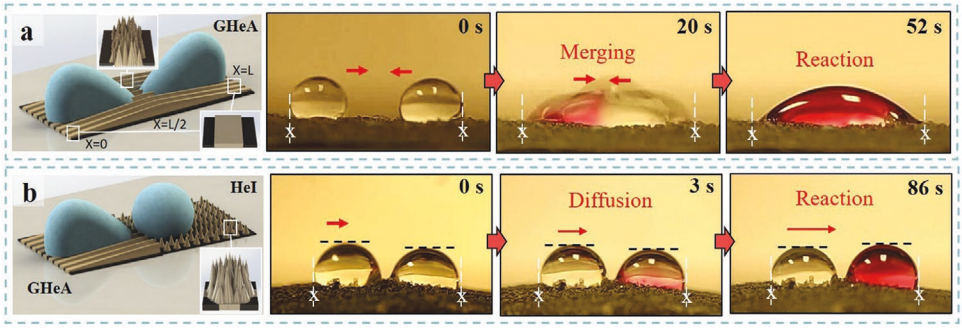

Figure 10. Design and time-sequent photos recording the processes of self-driven droplet reactions on two different surfaces fabricated by AAP: a) Bi-directional merging of droplets on a gradient HeA surface (more anisotropic center and less anisotropic edges). b) Unidirectional diffusion using a surface composed of gradient HeA structure on the left side and HeI structures on the right side.

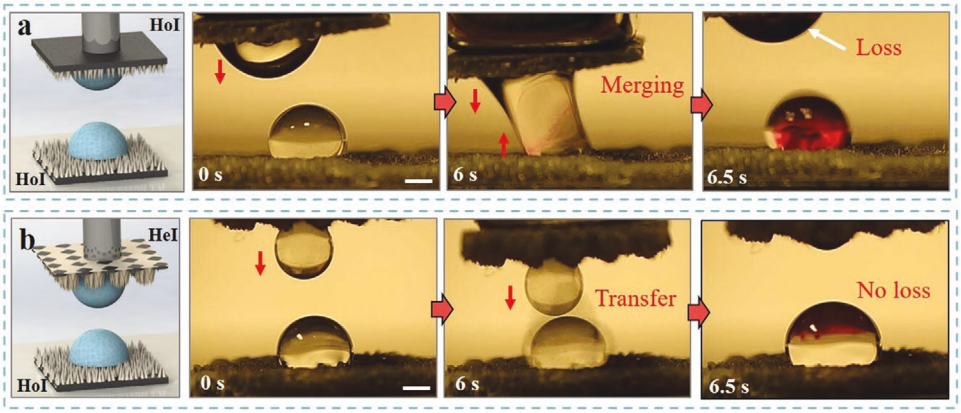

Figure 11. Design and time-sequent photos recording the processes of transferring a phenolphthalein droplet (top) into a KOH droplet (bottom) using two pairs of surfaces: a) *z*–direction reaction using HeI surfaces both on top and on bottom results in partial transfer. b) *z*–direction reaction using HeI surface on top and HoI surface on bottom results in nearly lossless transfer.

a bottom reaction chip (collector) for efficient droplet capture. The phenolphthalein droplet was dropped on the top and the KOH droplet on the bottom surfaces. In the first experiment (**Figure 11**a), the HoI surface was used as a top surface and brought close to the bottom HoI surface. A strong hysteresis was observed due to the same surface energy of both surfaces. As a result, while lifting the top surface, a large amount of phenolphthalein droplet remained on the top chip, indicating a significant loss during the transfer (see Movie S4, Supporting Information). In the second experiment (Figure 11b), when the superhydrophobic HeI surface was used as a top chip, the phenolphthalein droplet merged into KOH droplet without any hysteresis. Because the surface energy on HoI was much greater than that of the HeI surface, the phenolphthalein droplet was smoothly released from the HeI surface (6–6.5 s), achieving a nearly lossless transfer (see Movie S5, Supporting Information). In this case, transfer efficiency was calculated as 95% using the equation $\eta = (W_n - W_t)/W_b \times 100\%$, where W_n, W_t, and W_b, are the weight of the newly generated droplet, top droplet, and bottom droplet, respectively.

To summarize, experimental results, as discussed in Sections 3.3 and 3.4, showed that an automatic droplet spreading or merging without the requirement of any external power can be achieved using the multimaterial hierarchical surfaces developed in this study. Additionally, the rate of passive mixing and transfer efficiency can be controlled through preprogramming surface structure features by changing the acoustic assembly patterns and the exposure time during AAP fabrication. The results indicate the practical value of our AAP process in surface engineering for various biomedical applications, including detection, chemical reaction, microfluidics, nanoparticle synthesis, and directional liquid transport.

3.5. Test Case 3: Fog Harvesting

The fog harvesting ability of the fabricated surfaces was tested in laboratory conditions using a household humidifier. The setup was constructed based on our previously published work.[33] **Figure 12**a shows the schematic of the fog harvesting setup. A household humidifier (humidifying capacity: 50–210 mL h^{-1}, power: 20 W) was used to generate fog in the range of 1–40 µm in diameter, which is comparable with the fog sizes found in nature.[45] The surfaces with 20 × 20 mm^2 areas were placed on the sample holder perpendicular to the fog direction. The distance between the attached surface and the humidifier outlet was kept at 20 mm. The weight of the collected water in the container was measured using a digital balance (resolution: 0.1 mg). The quantitative measurements of the water collected from the generated fog were conducted by measuring the weight of collected water as a function of time.

The water collection experiment was conducted on three different surfaces (HoI, HeI, and HeA designs as discussed in Section 3.1 and shown in Figure 6) for 240 s, and the experimental results are plotted in Figures 12b,c. Among the three tested surfaces, the hydrophilic HoI surface showed the lowest water collection efficiency, that is, 178 mg within a 240 s cycle. HeI surface which is characterized by hydrophobic conical clusters surrounded by discrete hydrophilic particle patterns is more efficient (255 mg within a 240 s cycle) than the flat HoI surface. A sharp increase in the water collection efficiency (315 mg within a 240 s cycle) was observed in the experiment using an HeA surface, which can be attributed to the Laplace pressure and surface energy gradient of the HeA surface due to the hydrophilic groove design. The HeA surface was 1.2 and 1.8 times more efficient than HeI and HoI surfaces, respectively, clearly showing the superiority of anisotropic hierarchical surfaces with multimaterial composition.

The significant differences observed between the fog collection rates of various samples clearly show a strong influence of surface material composition pattern and surface topology on the water harvesting capabilities. The fog harvesting process typically includes water capture, collection, and transport.[46] As shown in Figure 12d, the water droplets were captured faster on HoI surface, followed by continuous nucleation owing to the hydrophilic nature of the surface. However, as the collection process continued, the captured droplets coalesced to form a bigger water droplet (see Movie S6, Supporting Information). No directional spreading or movement occurred because of the uniform surface energy. For the HeI surface shown in Figure 12e, the water

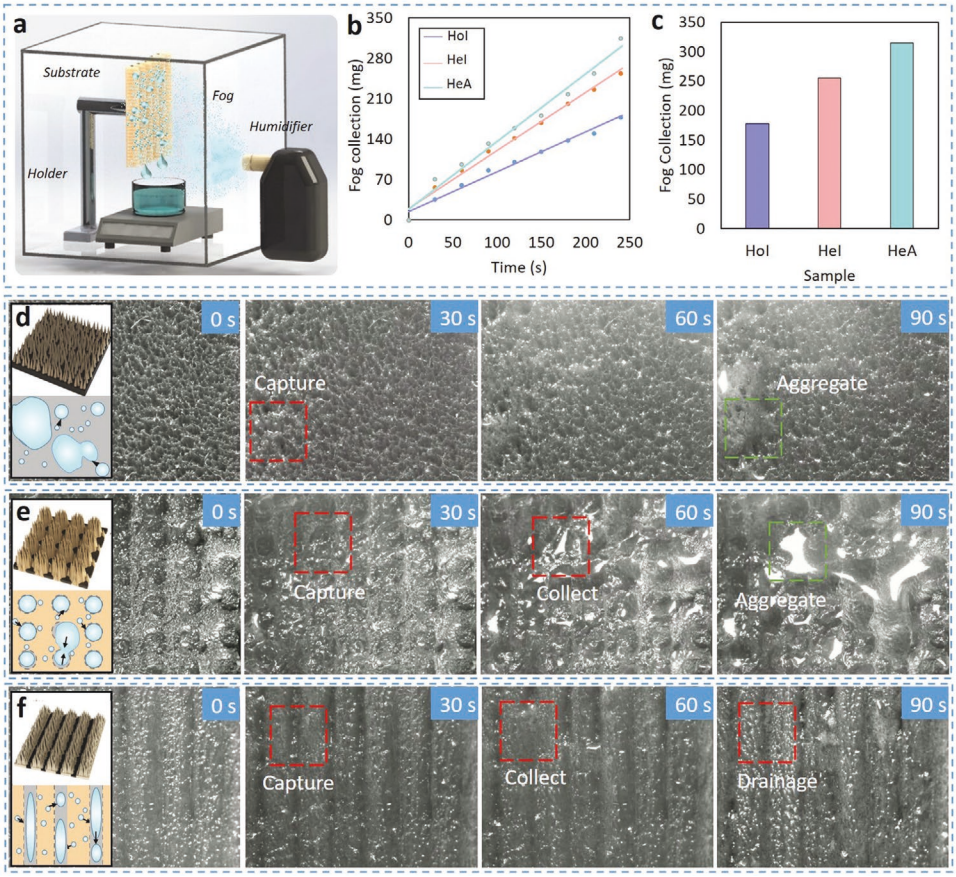

Figure 12. a) 3D schematic of the fog harvesting experiment setup. b) The weight of water collected every 30 s on different samples. c) The weight of water collected on different samples after 240 s. Schematic and time-lapse images of the fog-harvesting process on d) HoI surface. e) HeI surface. f) HeA surface.

droplets captured on the top surface of the conical clusters moved toward the bottom hydrophilic regions owing to the surface energy gradient. As a result, the directional self-clearing of the droplets from the hydrophobic (top of the cones) to hydrophilic (surrounding areas) regions allowed continuous growth of new droplets, leading to a higher fog collection rate than HoI surface. However, the collected water formed bigger water humps on the hydrophilic patterns, preventing continuous water collection (see Movie S7, Supporting Information).

For the HeA surface, at the beginning, similar to the HeI surface, the droplets were captured on the top of the hydrophobic conical plateau and collected on the hydrophilic groove region, forming humps separately, as shown in Figure 12f. As the collection process continued, the water droplets collected on the hydrophilic groove merged and drained down, owing to the Laplace pressure induced by grooved geometry. A new circulation starts right after transporting the collected water from the hydrophilic patterns (see Movie S8, Supporting Information). As a result, by accelerating surface regeneration using hydrophilic grooves, the fog collection efficiency on a HeA surface is enhanced remarkably. The material and topology contrast provided by the hydrophilic grooves and hydrophobic plateaus on the HeA surface allows the most efficient water collection and drainage along the groove direction.

4. Conclusion

In this study, we have developed a novel acoustic assembly photopolymerization process (AAP) to fabricate hierarchically-structured surfaces with spatially-varied material compositions. The relationship between the manufacturing process and *surface structure* was modeled and analyzed. The proposed manufacturing process is capable of producing isotropic or anisotropic surfaces with homogeneous or heterogeneous multimaterial distribution. The SEM image analysis showed that the fabricated multimaterial hierarchical surfaces consist of various hierarchical features, including clusters of cones, wrinkles, and parallel grooves. The geometry of the fabricated surface features can be controlled by varying multiple process parameter settings such as the supplied acoustic frequency, particle concentration in feedstock, and the duration of light exposure. The influence of the surface material composition pattern and surface topology was investigated on the static contact angle (θ from 76.72° to 160.54°), anisotropic wetting ($\Delta\theta$ from 0° to 87°), and fog harvesting capability(from 178 to 315 mg). To demonstrate the automatic hydrodynamic performance applications of the proposed AAP process, we implemented the developed surfaces for microreactor devices and fog harvesting. Droplets on the proposed surfaces can be continuously transported in

the desired direction, and efficient passive mixing is achieved without external actuation. The results demonstrate the effectiveness of integrating acoustic particle assembly into photopolymerization process for fabricating multimaterial surfaces with meso-micro-nanoscale hierarchical features.

We realized two limitations while conducting these experiments: limited scalability and material availability. In our current setup containing four piezoelectric plate arrangements and limited projection area, the maximum size of the fabricated surface is centimeter-scale (10 mm × 6 mm), which limits the large-scale production of multimaterial hierarchical surfaces. There are three options to address this challenge. Adding more piezoelectric plates and increasing the tank size might increase the scalability. Alternatively, other types of external fields could be explored. The small projection area challenge can be overcome by utilizing multiple projection units, as demonstrated by Zhou et al.[47] The second limitation is the availability of low viscosity material, which is required to eliminate viscous drag forces during acoustic patterning, as discussed in Section 3.1. A possible solution is to dilute the material used in this work with low viscosity solution, such as acetone.[29] Finally, the total fabrication time can be reduced further by reducing the exposure time. Several changes can be made to the hardware, such as increasing light intensity or selecting high power light source. In addition, polymers with a higher photosensitivity can be utilized.

Despite these limitations, the AAP fabrication is very fast and simple. It can produce multimaterial surfaces with meso-micro-nanoscale hierarchical features within seconds. Furthermore, the proposed AAP fabrication approach can be scaled up into SL processes to create 3D models with complicated geometry, for instance, multifunctional 3D microfluidic devices for droplet separation and tissue culture applications. Although this study only considered rectangular-shaped piezoelectric plates for simplicity, other piezoelectric plate shapes such as rings and circular discs can also be used in the proposed AAP setup.

To conclude, we believe that this newly developed AAP process could provide a new way to fabricate multimaterial hierarchical surfaces with preprogrammed functionalities for performing automatic tasks without requiring external power and bulk wiring systems. Combining multimaterial patterns and hierarchically-patterned topology would be an eco-friendly, sustainable, efficient, and powerful design strategy for next-generation device innovations, particularly, the preprogrammed automatic liquid controls demonstrated in this paper. Various applications, such as tissue culture and micro-assay chips, could benefit from the surface design, manufacturing, and characterization work presented in this paper. Future work will extend the work of automatic droplet control to flow control in microfluidic devices.

Supporting Information

Supporting Information is available from the Wiley Online Library or from the author.

Conflict of Interest

The authors declare no conflict of interest.

Data Availability Statement

The data that support the findings of this study are available in the Supporting Information of this article.

Keywords

acoustic assembly, fog harvesting, multimaterial surface structuring, photopolymerization, wettability

Received: September 6, 2022
Revised: October 3, 2022
Published online:

[1] M. J. Männel, N. Weigel, N. Hauck, T. Heida, J. Thiele, *Adv. Mater. Technol.* **2021**, *6*, 2100094.
[2] Y. Lee, K.-Y. Ju, J.-K. Lee, *Langmuir* **2010**, *26*, 14103.
[3] T. M. Block, S. Rawat, C. L. Brosgart, S. Francisco, *Biomaterials* **2017**, *104*, 69.
[4] S. Ben, T. Zhou, H. Ma, J. Yao, Y. Ning, D. Tian, K. Liu, L. Jiang, *Adv. Sci.* **2019**, *6*, 1900834.
[5] P. Guo, Y. Lu, K. F. Ehmann, J. Cao, *CIRP Ann.* **2014**, *63*, 553.
[6] A. Ghosh, R. Ganguly, T. M. Schutzius, C. M. Megaridis, *Lab Chip* **2014**, *14*, 1538.
[7] W.-L. Min, B. Jiang, P. Jiang, *Adv. Mater.* **2008**, *20*, 3914.
[8] K.-C. Park, P. Kim, A. Grinthal, N. He, D. Fox, J. C. Weaver, J. Aizenberg, *Nature* **2016**, *531*, 78.
[9] S. Dong, Y. Li, N. Tian, B. Li, Y. Yang, L. Li, J. Zhang, *ACS Appl. Mater. Interfaces* **2018**, *10*, 41878.
[10] C. Peng, Z. Chen, M. K. Tiwari, *Nat. Mater.* **2018**, *17*, 355.
[11] J. Xu, Y. Hou, Z. Lian, Z. Yu, Z. Wang, H. Yu, *Nanomaterials* **2020**, *10*, 2140.
[12] P. Wang, T. Zhao, R. Bian, G. Wang, H. Liu, *ACS Nano* **2017**, *11*, 12385.
[13] Y. Li, S. Dai, J. John, K. R. Carter, *ACS Appl. Mater. Interfaces* **2013**, *5*, 11066.
[14] W. Liu, P. Fan, M. Cai, X. Luo, C. Chen, R. Pan, H. Zhang, M. Zhong, *Nanoscale* **2019**, *11*, 8940.
[15] Y. Lu, L. Yu, Z. Zhang, S. Wu, G. Li, P. Wu, Y. Hu, J. Li, J. Chu, D. Wu, *RSC Adv.* **2017**, *7*, 11170.
[16] K.-M. Lee, C.-V. Ngo, J.-Y. Jeong, E.-C. Jeon, T.-J. Je, D.-M. Chun, *Coatings* **2017**, *7*, 194.
[17] L. Peng, S. Zhou, B. Yang, M. Bao, G. Chen, X. Zhang, *ACS Appl. Mater. Interfaces* **2017**, *9*, 24339.
[18] S. Liu, X. Zhang, S. Seeger, *ACS Appl. Mater. Interfaces* **2019**, *11*, 44691.
[19] M. Ifires, T. Hadjersi, R. Chegroune, S. Lamrani, F. Moulai, M. Mebarki, A. Manseri, *J. Alloys Compd.* **2019**, *774*, 908.
[20] A. Stein, F. Li, N. R. Denny, *Chem. Mater.* **2008**, *20*, 649.
[21] Y. Yang, X. Li, X. Zheng, Z. Chen, Q. Zhou, Y. Chen, *Adv. Mater.* **2018**, *30*.
[22] K. M. Lichade, Y. Jiang, Y. Pan, *J. Manuf. Sci. Eng.* **2021**, *143*, 081002.
[23] L. Lu, P. Guo, Y. Pan, *J. Manuf. Sci. Eng.* **2017**, *139*, 071008.
[24] X. Li, W. Shan, Y. Yang, D. Joralmon, Y. Zhu, Y. Chen, Y. Yuan, H. Xu, J. Rong, R. Dai, Q. Nian, Y. Chai, Y. Chen, *Adv. Funct. Mater.* **2021**, *31*, 2003725.
[25] K. M. Lichade, Y. Pan, *J. Manuf. Sci. Eng.* **2021**, *143*, 104501.
[26] K. M. Lichade, S. Hu, Y. Pan, *Manuf. Lett.* **2021**, *31*, 110.
[27] Y. Yang, Z. Chen, X. Song, Z. Zhang, J. Zhang, K. K. Shung, Q. Zhou, Y. Chen, *Adv. Mater.* **2017**, *29*, 1605750.
[28] L. Lu, X. Tang, S. Hu, Y. Pan, *3D Print. Addit. Manuf.* **2018**, *5*, 151.
[29] S. Asif, P. Chansoria, R. Shirwaiker, *J. Manuf. Processes* **2020**, *56*, 1340.

[30] J. Greenhall, B. Raeymaekers, *Adv. Mater. Technol.* **2017**, *2*, 1700122.
[31] S. R. Lakhotia, M. Mukhopadhyay, P. Kumari, *Sep. Purif. Technol.* **2019**, *211*, 98.
[32] R. Contreras-Montoya, A. B. Bonhome-Espinosa, A. Orte, D. Miguel, J. M. Delgado-Lopez, J. D. G. Duran, J. M. Cuerva, M. T. Lopez-Lopez, L. Álvarez de Cienfuegos, *Mater. Chem. Front.* **2018**, *2*, 686.
[33] K. M. Lichade, Y. Pan, *North Am. Manuf. Res. Conf.* **2022**, *33*, 644.
[34] D. E. Yunus, S. Sohrabi, R. He, W. Shi, Y. Liu, *J. Micromech. Microeng.* **2017**, *27*, 045016.
[35] B. Elder, R. Neupane, E. Tokita, U. Ghosh, S. Hales, Y. L. Kong, *Adv. Mater.* **2020**, *32*, 1907142.
[36] M. Prisbrey, J. Greenhall, F. Guevara Vasquez, B. Raeymaekers, *J. Appl. Phys.* **2017**, *121*, 014302.
[37] J. Chi, X. Zhang, Y. Wang, C. Shao, L. Shang, Y. Zhao, *Mater. Horiz.* **2021**, *8*, 124.
[38] H. Li, A. Li, Z. Zhao, M. Li, Y. Song, *Small Struct.* **2020**, *1*, 2000028.
[39] K. Kowsari, B. Zhang, S. Panjwani, Z. Chen, H. Hingorani, S. Akbari, N. X. Fang, Q. Ge, *Addit. Manuf.* **2018**, *24*, 627.
[40] K. M. Lichade, E. B. Joyee, Y. Pan, *J. Manuf. Processess* **2021**, *65*, 20.
[41] I. S. Kiyomura, F. Nascimento, A. Cunha, E. M. Cardoso, *Proc 23rd ABCM Int Congr Mech Eng* **2015**.
[42] A. Davanlou, R. Kumar, *Microfluid. Nanofluid.* **2015**, *19*, 1507.
[43] A. Li, H. Li, Z. Li, Z. Zhao, K. Li, M. Li, Y. Song, *Sci. Adv.* **2020**, *6*, eaay5808.
[44] L. Sun, F. Bian, Y. Wang, Y. Wang, X. Zhang, Y. Zhao, *Proc. Natl. Acad. Sci. USA* **2020**, *117*, 4527.
[45] Y. Yao, C. Machado, Y. Jiang, E. Feldman, J. Aizenberg, K.-C. Park, *arXiv:1911.10603* **2019**.
[46] M. Aliabadi, A. Zarkesh, M. Mahdavinejad, *Mater. Res. Express* **2018**, *5*, 115502.
[47] C. Zhou, Y. Chen, in *36th Design and Automation Conference*, Vol. *1*, ASME, Montreal, QC, Canada **2010**, p. 439, https://doi.org/10.1115/DETC2010-28922.